ELSEVIER

Assessment of potential service-life performance for MarBN steel power plant header under flexible thermomechanical operations

M. Li[a,*], A. Benaarbia[b], A. Morris[c], W. Sun[a]

[a] Department of Mechanical, Materials and Manufacturing Engineering, University of Nottingham, Nottingham, Nottinghamshire NG7 2RD, UK
[b] Arts et Métiers, CNRS, Université de Lorraine, LEM3, F-57000 Metz, France
[c] EDF Energy, West Burton Power Station, Retford, Nottinghamshire DN22 9BL, UK

ARTICLE INFO

ABSTRACT

This paper is concerned with the service-life assessment of 9Cr steels superheater outlet steam header subjected to realistic subcritical and future ultra-super critical flexible operating conditions. The proposed methodology is achieved via a combined program of high temperature strain-controlled fatigue tests, temperature- and time-dependent unified viscoplastic model for thermomechanical fatigue analysis, and Smith-Watson-Topper critical plane criterion for multi-axial life prediction. Samples of idealised operational transients with particular attention on the starting-up cycle is fully coupled with the computational modelling of header component for the high temperature performance assessment. The predicted results indicate that: (i) the header shell inner-bore saddles at weld regions are the critical locations that lead to earlier potential fatigue crack initiation, and (ii) the predicted lifetime under subcritical conditions correlates reasonably with the industrial experience. A steam header manufactured from MarBN operating under ultra-super critical condition is shown to have comparable life performance with the P91 header operating under subcritical condition.

1. Introduction

The most important challenges facing next generation power plants include improving efficiency and reducing CO_2 emissions, whilst maintaining safe and reliable operation. Accordingly, additional flexible conditions are needed in the power plant to accommodate rapid load variation of fossil-fired power plants, which will cause lifetime reduction of component due to alternating stresses during transient processes [1,2]. The thermodynamic efficiency of fossil-fired power plants can be improved by increasing the pressure and boiler outlet temperature, i.e. operating above 600 °C is termed as ultra-super critical (USC) [3]. Fig. 1 illustrates the average starts per year on a 500 MW unit (mainly flexible operation) during the last 21 years in a fossil-fired power plant in the UK [4]. Key issues however still exist, in relation to life prediction to guide the scope of periodic outage inspections of critical high temperature components (typically fabricated from a range of ferritic steels and 9Cr steels, such as P91). From a material perspective the challenges also include: (i) extrapolation to

more realistic plant operations resulting in creep-fatigue interaction (CFI) deformation, and (ii) thermomechanical fatigue (TMF) due to the combination of flexible operation and complex thick-wall component geometries [5–9].

MarBN (MARtensitic 9Cr steel strengthened by Boron and Nitrides) has been identified as a candidate material, originally designed for increased temperature operation of thick section boiler components for next generation USC applications above 600 °C. It has been reported in [10] that the boron and nitrogen stabilise the lath martensitic microstructure and reduce the rate of Ostwald ripening for $M_{23}C_6$ carbides near prior austenite grain boundaries (PAGBs) for improved the mechanical strength compared with the existing 9Cr steels in short-term creep, high temperature low cycle fatigue (LCF) and CFI [11–16], for example, Barrett *et al.* [11] and O'Hara *et al.* [15,16] experimentally reported that the MarBN steel exhibited an increased stress-range of approximately 20% compared with the P91 steel. LCF and CFI tests on MarBN under high temperature were recently conducted by Benaarbia *et al.* [13] and O'Hara *et al.* [15,16], which indicates that the additional

---

* Corresponding author.
  E-mail address: Ming.li1@nottingham.ac.uk (M. Li).

Nomenclature

$\Delta\epsilon$	strain-range	R	isotropic hardening stress
$\dot{\epsilon}$	strain-rate	R'	drag stress
ϵ_T	total strain tensor	F_y	von-Mises yield function
$\boldsymbol{\epsilon}_e$	elastic strain tensor	ϕ_{vp}	power-law function
$\boldsymbol{\epsilon}_{vp}$	viscoplastic strain tensor	Σ_{vM}	the second invariant
$\dot{\boldsymbol{\epsilon}}_{vp}$	viscoplastic strain-rate tensor	k	cyclic yield stress
$\Delta\epsilon_I$	maximum principal strain-range	ω	viscoplastic resistance
η	viscoplastic multiplier	χ	viscoplastic exponent
$\dot{\eta}$	viscoplastic multiplier rate	A_i	linear hardening term
$\boldsymbol{\sigma}$	stress tensor	$\boldsymbol{B}_i$	dynamic recovery term
$\dot{\boldsymbol{\sigma}}$	stress rate tensor	$\boldsymbol{C}_i, \varphi$	temperature-rate term
$\boldsymbol{\sigma}'$	deviatoric stress tensor	a_i, b_i	kinematic hardening parameters
σ_v	viscous stress	c, d	isotropic hardening parameters
σ_I	maximum principal stress	σ_f	fatigue strength
E	Young's modulus	g	fatigue strength exponent
$\boldsymbol{C}_e$	fourth-order elastic stiffness tensor	ϵ'_f	fatigue ductility coefficient
$\boldsymbol{X}$	non-linear kinematic stress	h	fatigue ductility exponent
		N_f	number of cycles to failure
		T	absolute temperature

short-term creep is detrimental to the fatigue life and cyclic strength. Additionally, different kinds of fatigue tests with varied hold periods were carried out in [13] indicating the effects of applied loadings on the resultant microstructural evolution of MarBN at high temperature. Besides the work mentioned above, the authors are not aware of any other published experimental work on MarBN under high temperature LCF and CFI with the purpose to explore the possible future USC application by comparing with existing 9Cr steels.

High temperature and pressure components manufactured from P91 steel have received a lot of attention to accommodate experimental data in computational models, in order to investigate the consequent deformation behaviors. However, only few studies have been carried out to assess the lifetime of such component under flexible operation. Work carried out in [7–9,17–19] has reported that the steam headers are more susceptible to CFI and TMF due to flexible operation, leading to microstructural degradation and reduction in component life. Rouse et al. [20] proposed a Chaboche type based model, considering the effect of variable steam flow conditions within the header component on

Fig. 1. Typical unit average starts over 21 years for a UK conventional fossil-fired power plant.

the stress-strain evolution at the localized region. Finite element (FE) analyses have been performed in [21] to study the effect of different thermal cycles on fatigue life of steam headers without explicitly considering the viscous effect of power plant material for the operation at stabilized maximum internal loads. T. Hassan et al. [22] employed a unified viscoplasticity model based on continuum damage mechanics (CDM) to evaluate the CFI damage behaviour and predict service-life of a header component. The two-layer viscoplasticity model of Farragher et al. [5] was adopted within the FE code for TMF analysis of a P91 header and the service-life were predicted through a critical-plane approach, although the material models adopted in [5,22] were not calibrated with CFI experimental data of the candidate material under anisothermal conditions. In summary, the previous studies mainly focus on the analysis of mechanical deformation of header component by neglecting the idealised loading histories of flexible operation and viscous effect of the candidate material at varied temperatures, however, the lifetime assessment during flexible transient processes coupled with unified thermodynamic viscoplastic material law and experimental data was scarce. Therefore, in order to realise the potential performance of MarBN for the future USC power plant application, a unified viscoplasticity framework, which represents both the viscoplastic responses and temperature-dependent material behaviors under flexible thermomechanical operation for lifetime assessment is required.

The first part of this paper introduces the MarBN steel, LCF and CFI experimental results, followed by an anisothermal temperature- and time-dependent viscoplasticity material modelling framework including the material parameter identification and calibration. The methodology for the service-life prediction of a superheater steam header based on high temperature viscoplastic analyses is then presented. One of the key objectives of the current work is to incorporate the uniaxial experimental fatigue data of the material under investigation with representative flexible operation data in a numerical model to explore the possible future service-life performance of MarBN at the component level. The findings covering failure locations and life estimation are provided with a comparison between current P91 steels in-service at subcritical steam condition and MarBN for possible future USC applications.
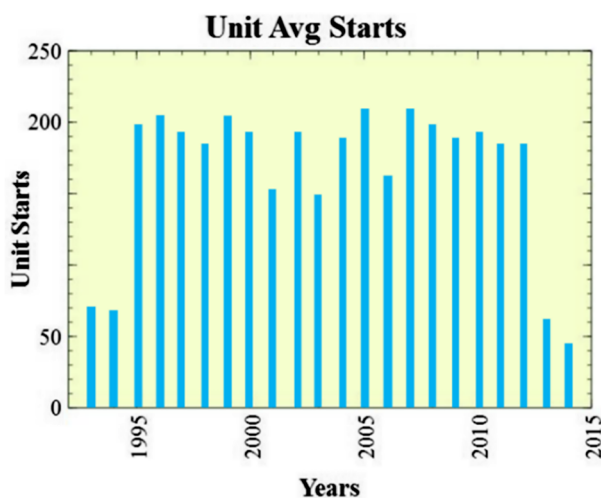
Table 1
Chemical composition of the investigated tempered MarBN (all elements are in wt.%, B and N are in ppm).

C	Si	Mn	P	S	Cr	Mo	Ni	Al	B	Co	W	V	Nb	N	Cu
0.1	0.45	0.54	0.012	0.004	8.74	0.05	0.14	0.007	120	3.02	2.53	0.21	0.06	0.018	0.04

2. Material and experimental program

2.1. Material

MarBN steel exhibits a hierarchical arrangement, comprising of prior austenite grains (PAGs), packets, blocks, and laths. The PAGs can be further sub-divided into packets with block including lath distributions with low angle boundaries [12,23,24]. The chemical composition of the investigated tempered MarBN steel is given in Table 1. The test specimens were extracted from forged bars which were obtained after normalizing tempering at 1200 °C for 4 h followed by a tempering treatment at 765 °C for 3 h.

2.2. Test program

The high temperature LCF and CFI tests were performed using a Tinius Olsen H25KS DSCCTOL 25 KN load testing machine (see Fig. 2) equipped with a Severn Thermal Solution SF2107 high-temperature furnace. Fig. 3(a) shows the dimensions of the specimens which have a uniform gauge section of 5 mm in diameter and 10 mm in length. Fully reversed uniaxial strain-controlled tests with and without dwell-periods were conducted with trapezoidal waveform and sawtooth triangular waveform, as shown in Fig. 3(b) and (c), respectively. Note that the trapezoidal waveforms with dwell-periods (2.5 h hold for the initial cycle and 30 mins hold for the subsequent cycles) are hereafter referred to DWT for CFI test, while the sawtooth triangular waveforms without dwell periods are hereafter referred to SWT for LCF test. The test matrix adopted in the current work is given in Table 2, and the associated mechanical responses used for material parameter identification can be found in [6,13]. The P91 LCF and CFI tests previously carried out by Saad *et al.* [25,26] are also given in Table 2 for the comparison of the high temperature service-life performance of the MarBN and P91 headers. All the tests were performed at a strain-range, $\Delta \epsilon$, of $\pm 0.5\%$
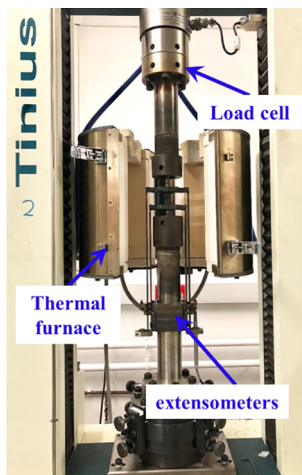

Fig. 2. The experimental setup based on Tinius Olsen H25KS electromechanical testing machine consisting of a ± 25 kN pancake style load cell and a Severn Thermal Solutions SF2107 furnace.

and a strain-rate, $\dot{\epsilon}$, of 0.01%s^{-1}.

Fig. 4(a) and (b) show an example of comparisons of measured stress-strain hysteresis loops of MarBN steel subjected to SWT and DWT conditions, Fig. 4(a) for the initial cycle ($N = 1$), and Fig. 4(b) for the half-life ($N_f/2$) cycle. It can be seen from Fig. 4(a) that the inelastic strain-range of DWT is larger than SWT due to the additional dwell period, leading to accelerated material softening and damage evolution which can be seen in Fig. 4(b) of half-life cycle. The continuous cyclic softening of MarBN is described by the variation of maximum stress of every cycle against the number of cycles in Fig. 4(c). It clearly can be concluded from Fig. 4(c) that the additional short-term dwell is detrimental to fatigue life, cyclic strength, and accelerate the rate of cyclic softening by comparing with LCF tests (SWT tests).

3. Constitutive model and numerical implementation

3.1. Unified anisothermal viscoplasticity model

The Chaboche material model [27,28] with some essential extensions [29] is used in the current work, to represent the cyclic viscoplastic behavior of the MarBN steel. This model has already been successfully applied for martensitic steels under high temperature conditions [30,31], and is now extended to account for both temperature-dependent and time-dependent MarBN behaviors under anisothermal conditions. The combination of such two parallel mechanisms is the prerequisite for the component analysis in the power plant industry under flexible thermomechanical operation.

In the unified viscoplasticity model, it is assumed that the material behavior can be described by both elastic and viscoplastic deformations, where the later is a combined contribution from both creep and cyclic plasticity. Hence, under small-strain framework, the total strain tensor, ϵ_T, can be divided into both a recoverable elastic component, ϵ_e, and an irreversible viscoplastic component, ϵ_{vp}, with the stress rate tensor, $\dot{\sigma}$, being determined through the Hooke's law such that

$$\dot{\sigma} = \mathbf{C}_e : (\dot{\epsilon}_T - \dot{\epsilon}_{vp}) \tag{1}$$

where $\mathbf{C}_e$ stands for the fourth-order elastic stiffness tensor. The unified viscoplastic model adopted in this work includes both non-linear kinematic and isotropic hardening rules stresses, X and R, for the cyclic plastic behavior as well as a power-law function, ϕ_{vp}, for the viscous behavior. Thus, the inelastic viscoplastic strain-rate flow rule, $\dot{\epsilon}_{vp}$, based on the von-Mises yield function, F_y, can be defined such that:

$$F_y = \Sigma_{vM}(\sigma' - X) - R(T, \eta(T)) - k(T), \tag{2}$$

$$\dot{\epsilon}_{vp} = \dot{\eta} \frac{\partial F_y}{\partial \sigma} = \frac{3}{2} \frac{(\sigma' - X)}{\Sigma_{vM}(\sigma' - X)} \phi_{vp}(\dot{\eta}, X, R; T), \tag{3}$$

where $k(T)$ represents the initial temperature-dependent cyclic yield stress, while X and R stand for the non-linear kinematic hardening back-stress tensor and the isotropic hardening stress, respectively. $\Sigma_{vM}(\sigma' - X) = \sqrt{\frac{3}{2}(\sigma' - X):(\sigma' - X)}$ denotes the second invariant of the stress tensor, σ, while the prime symbol σ' stands for the deviator part of the stress tensor σ. In the viscoplastic rate form (Eq. (3)),
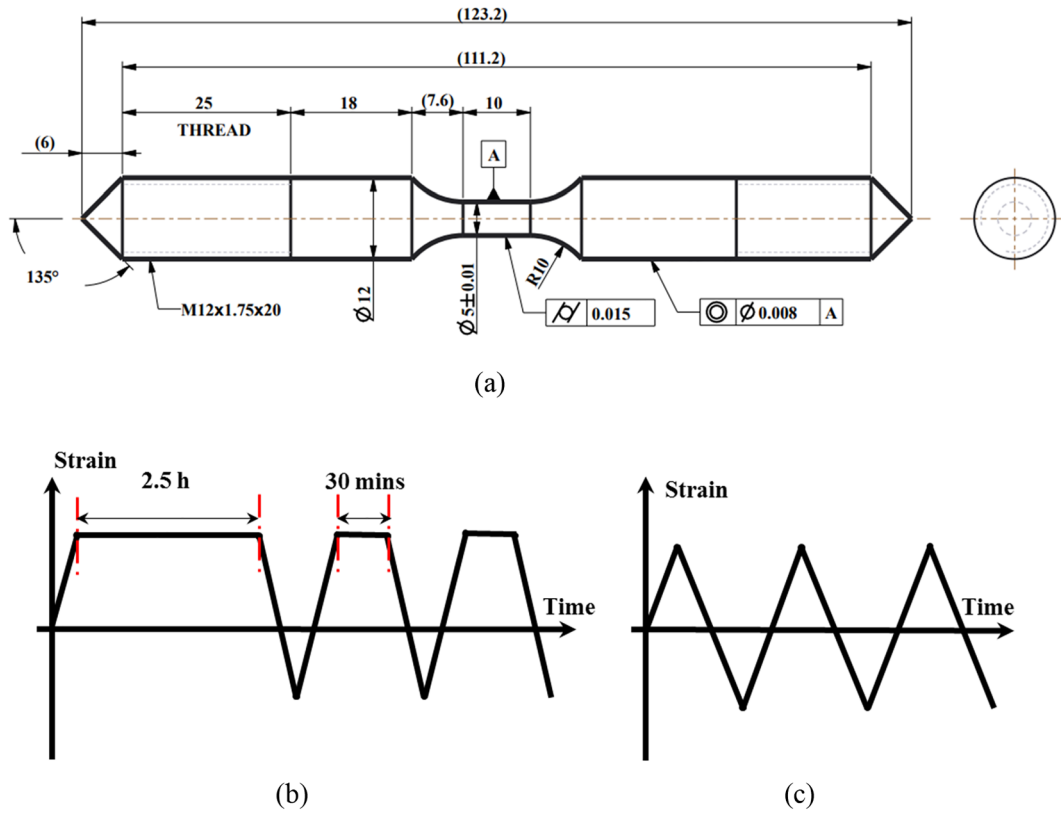
(a)

(b)

(c)

Fig. 3. (a) Dimensions of the investigated specimens (mm); (b) DWT loading pattern used for the CF experiments, and (c) SWT loading pattern used for the LCF experiments.

$\dot{\eta}$ represents the inelastic viscoplastic multiplier rate. The viscous function, ϕ_{vp}, chosen hereafter obeys the power-law form to capture the viscous effect observed above and below the yielding. This function is defined such that

$$\phi_{vp} = (F_y/\omega(T))^{\chi(T)}, \qquad (4)$$

where $\omega(T)$ and $\chi(T)$ are the temperature-dependent viscoplastic resistance and exponent, respectively.

Two kinematic back-stress components, X_1 and X_2, were selected in the constitutive model to describe the motion of the yield surface and account for the Bauschinger effect in materials, while X_1 represents the kinematic hardening produced after the elastic portion of loading and X_2 accounts for the kinematic hardening due to the later stages of strain hardening. An Armstrong-Frederick form has been used to describe the non-linear evolution of the kinematic hardening, including linear hardening term, $A_i(T)\ \dot{\epsilon}_{vp}$, and dynamic recovery term, $-\ B_i(T)\dot{\eta}$, coupled with an additional temperature-rate term, $C_i(T)\dot{T}$. The Chaboche kinematic hardening decomposition of the elementary back-

stress is formulated as follows

$$\dot{X} = \dot{X}_1 + \dot{X}_2, \qquad (5)$$

$$\dot{X}_i(T) = A_i(T)\ \dot{\epsilon}_{vp} - B_i(T)\dot{\eta} + C_i(T)\dot{T}, \qquad (6)$$

$$A_i(T) = \frac{2}{3}a_i(T)b_i(T), \qquad (6.1)$$

$$B_i(T) = a_i(T)X_i(T), \qquad (6.2)$$

$$C_i(T) = \left(\frac{1}{a_i(T)}\frac{\partial a_i(T)}{\partial T} + \frac{1}{b_i(T)}\frac{\partial b_i(T)}{\partial T}\right)X_i(T), \qquad (6.3)$$

where $a_i(T)$ and $b_i(T)$ are kinematic hardening temperature-dependent functions. A non-linear anisothermal form for the isotropic hardening stress, R, is employed hereafter to account for the continuous decelerated cyclic softening. This form can be written such that

$$\dot{R}(T, \eta(T)) = D(T, \eta(T))\dot{\eta} + \varphi(T, \eta(T))\dot{T}, \qquad (7)$$

$$D(T, \eta(T)) = (c(T) - R(T, \eta(T)))d(T), \qquad (7.1)$$

$$\varphi(T, \eta(T)) = \left(\frac{1}{c(T)}\frac{\partial c(T)}{\partial T} + \frac{1}{d(T)}\frac{\partial d(T)}{\partial T}\right)R(T, \eta(T)), \qquad (7.2)$$

in which $c(T)$ and $d(T)$ are isotropic hardening temperature-dependent functions to be determined. These terms represent, respectively, the saturated value of the isotropic softening stress with increasing viscoplastic strain and the decay-rate that leads to the softening saturation.

Table 2
The selected experimental tests conducted on MarBN and P91 steels [13,25,26].

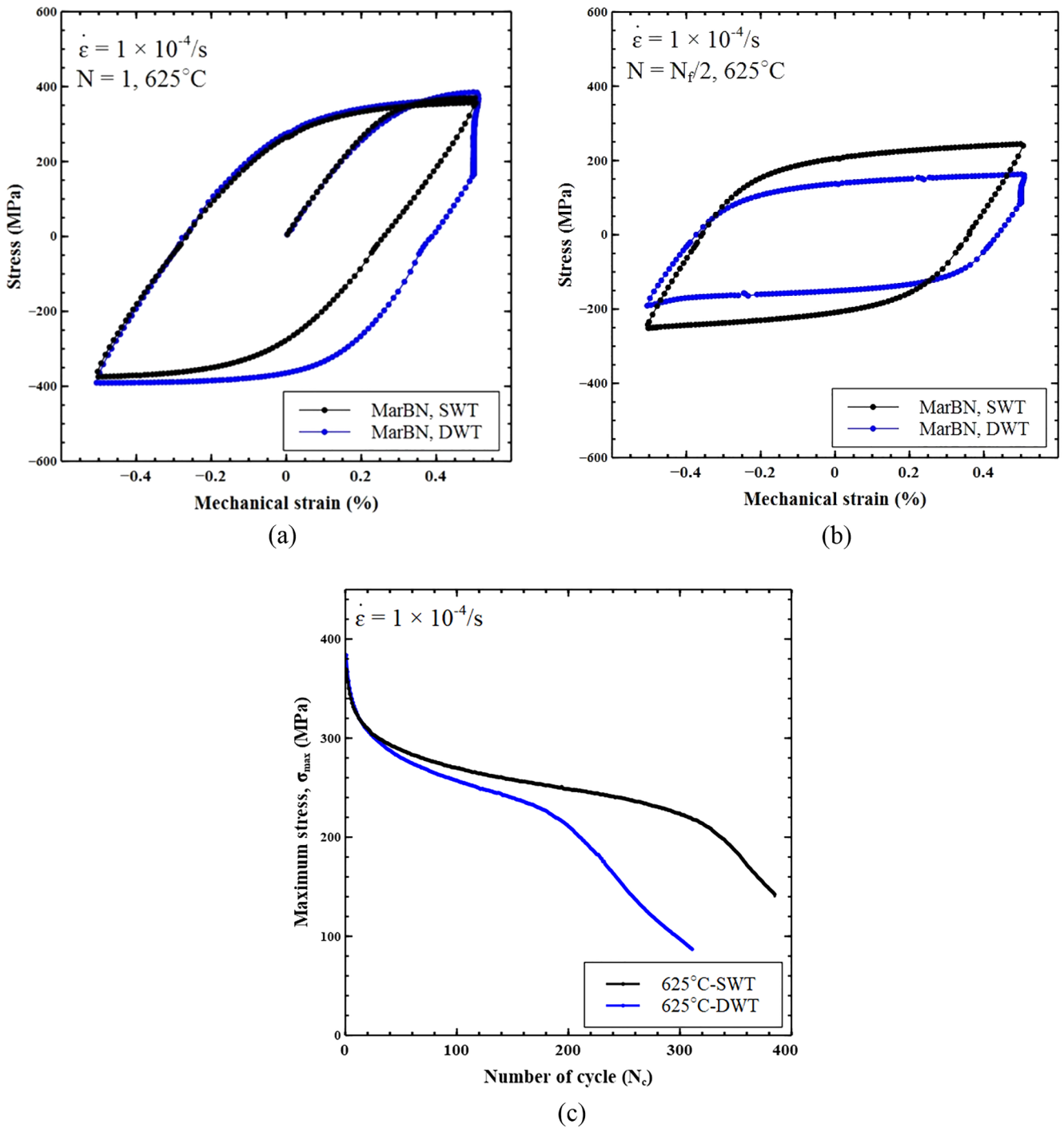| Material	Strain-range $\triangle\epsilon$ (%)	Strain-rate $\dot{\epsilon}$ (%)	Temperature (°C)	Waveforms
MarBN	± 0.5	0.01	400	SWT
			625, 650, 675	SWT, DWT
P91 [25,26]			400, 500, 600	SWT, DWT

Fig. 4. Comparisons of measured results of MarBN between SWT and DWT at 625 °C (a) Stress-strain responses for the initial cycle, (b) Stress-strain responses for the half-life cycle, (c) Cyclic evolution of maximum stress for SWT and DWT tests, respectively.

The aforementioned constitutive model is implemented in a FE code ABAQUS [32] through a home-made user subroutine (UMAT) [30,31].

3.2. Determination of the material parameters

The constitutive parameter identification process for the MarBN steel follows the work described in [6,30], based on the cyclic SWT and DWT data over a range of test temperatures. A total of 11 parameters involved in the adopted unified viscoplastic model are separated into three groups consisting of elastic parameters, non-linear viscous parameters, and cyclic plasticity parameters. The material parameters such as Young's modulus, E, and initial yield stress, k, are estimated through

the 1st cycle of LCF test data. It should be noted that the value of k, is defined as half the distance of the linear vertical region when plotting plastic strain versus stress following the approach described by Lemaitre and Chaboche [6,33], while Poisson's ratio is assumed to be 0.3. The remaining parameters are elaborated using a step-by-step procedure as introduced in [30].

The viscous parameters at the selected temperatures are obtained by plotting $\ln(\sigma_v)$ vs. $\ln(\dot{\eta})$ based on Cottrel's stress partition [25] from the stress relaxation region of the DWT data such that $\ln(\sigma_v) = \chi^{-1}\ln(\dot{\eta}) + \ln(\omega)$, as shown in Figs. 5 and 6. It is worth noting that the rate of the viscoplastic multiplier, $\dot{\eta}$, is considered to be equal to $\dot{\eta} = -\dot{\sigma}/E$.

The isotropic softening parameters, c and d, are identified by plotting the drag stress, R, vs. the viscoplastic multiplier, η, estimated such that $\eta \approx 2N\Delta \epsilon_{vp}$, where N is for the number of cycles. Due to the continued cyclic softening observed in the MarBN steel behavior, the saturated value of softening, c, is taken to be the isotropic stress, R, just prior to the onset of failure. The parameter, d, which describes the decay-rate of R, is fitted to the experimental data, as illustrated in Fig. 7(a). In addition, the kinematic hardening parameters are obtained from the process outline in [6,18,30]. To do so, the hardening parameters, a_2 and b_2, associated with the second component, X_2, are identified from the intercept and the slope of $\ln(\partial(\sigma - R)/\partial \epsilon_{vp})$ vs. the viscoplastic strain, ϵ_{vp}. Assuming that the first back-stress has a negligible effect on the later hardening, the process is then repeated to determine a_1 and b_1 by plotting $\ln(\frac{\partial(\sigma - R - X_2)}{\partial \epsilon_{vp}})$ vs. the viscoplastic strain, ϵ_{vp}, for the initial stages of hardening, as presented in Fig. 7(b). It is worth noting that the focus of the current work is confined to the investigation of the MarBN steel behavior until the "supposed" stabilized cycle, thereby the damage mechanisms are not captured by the constitutive model.

3.3. Calibration of the viscoplastic constitutive model

The capability of the proposed unified viscoplastic model is further checked via the predicted stress-strain hysteresis loops, by uniaxial implementation of the model within a standalone multi-axial UMAT code [30,31], for a strain-rate of 0.01%/s and an applied strain-range of ± 0.5%. The results in Fig. 8(a), (c) and (e) show the ability of the model to predict the mechanical responses at the selected test temperatures by comparing the predicted hysteresis loops to the DWT experimental data at the 2nd, 50th and 100th cycles, respectively.
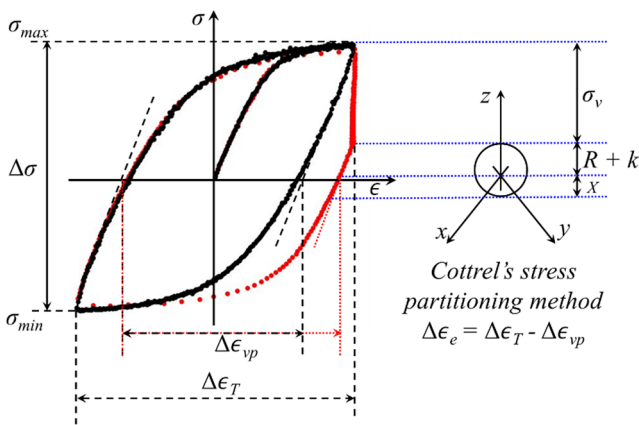

Fig. 5. Schematic hysteresis loops for both SWT and DWT with tensile hold periods, showing the Cottrel's stress partition.
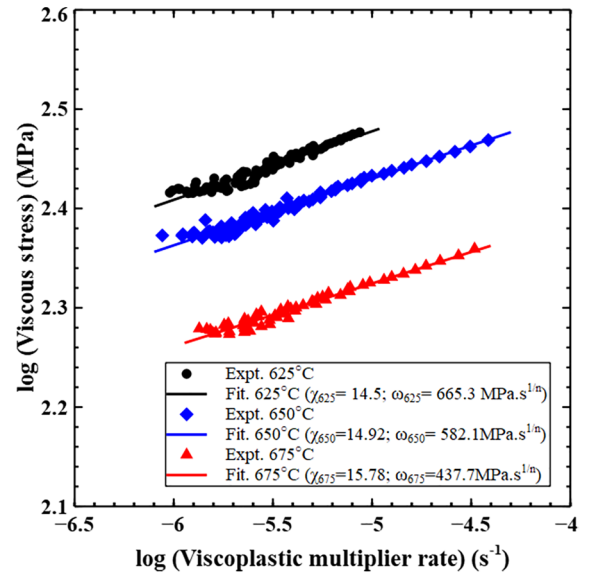

Fig. 6. Identification of the viscous parameters for the MarBN steel at the three selected temperatures based on the DWT data.

Fig. 8(b), (d) and (f) compare the simulated temporal stress evolution with the DWT experimental data for the selected fatigue cycles. The results show an excellent agreement with the experimental data; the model captures both the decelerated relaxation behavior and cyclic softening. Linear relationships of the material parameters with respect to the test temperatures were thus considered and summarised in Table 3. These formulations were then chosen to carry out the FE analyses for the superheater header. The P91 parameters under subcritical conditions were obtained from the authors' previous works [25,26].

4. Methodology for multi-axial service-life prediction

4.1. Thermomechanical loading histories

The main objective of the current work is (i) to provide a service-life prediction strategy for a superheater steam header at the critical locations subjected to complex thermomechanical loading, and (ii) to evaluate and then compare the high temperature mechanical performances of both P91 and MarBN headers under subcritical and USC conditions, respectively. Fig. 9(a) illustrates five typical thermomechanical cycles from operating plant showing time-dependent steam temperature and pressure histories obtained just downstream from an Électricité de France (EDF) superheater outlet header.

A simplified representative cycle is proposed in Fig. 9(b). This idealised cycle is used hereafter to capture the salient features of loading histories for the assessment of subsequent deformation behavior of a high temperature pressurised steam header. The initial part of the 'representative' cycle simulates a starting-up and the corresponding temperature increases from 181 °C to 467 °C after 2.5 h. This first part is followed by an exceptional cooling-down between 2.5 h and 4.65 h, when sudden reductions in steam temperature occur. Then, a dwell plateau of ~17 h occurs, hovering around a mean value of approximately 550 °C with ± 10 °C fluctuation. The temperature subsequently returns to 438 °C after 5.7 h with linear cooling-rates. The steam pressure history follows almost the identical pattern as the temperature
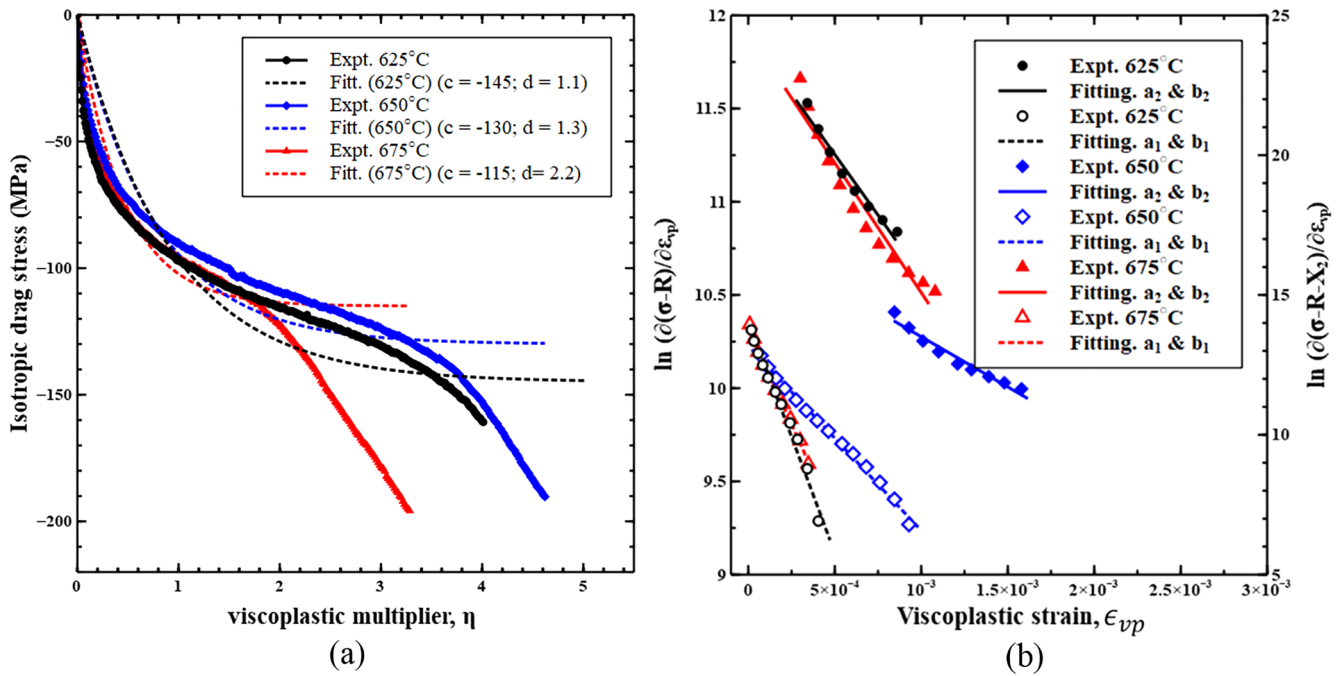
Fig. 7. Identification of the (a) isotropic parameters, and (b) kinematic hardening parameters for the MarBN steel at the three selected temperatures.

history (in-phase), initially increasing from 0 to 15.9 MPa over 8.75 h with short dwell periods. The pressure is then held almost constant for 15 h during which the temperatures eventually stabilize. When the power plant enters cool-down phase the pressure decreases to 0 over 1 h as the plant shuts down. The idealised load profile without consideration of the frequent thermal transients during dwell periods, as given in Fig. 9(b), will be coupled within the FE analysis.

Different combinations of internal pressure and thermal cycle conditions are considered during the FE modelling in order to assess the high temperature performance of both P91 and MarBN headers:

(i) Typical flexible operating condition for the maximum pressure and temperature of 15.9 MPa and 550 °C for P91, referred to as 'subcritical' operating conditions based on the loading cycle in Fig. 9(b).

(ii) Scaling the subcritical operating conditions (same loading pattern as shown in Fig. 9(b)) with a significant increase in peak operating pressure and temperature of 22 MPa and 650 °C [34] for MarBN steel operating in future 'USC' conditions.

4.2. Finite element model of steam header

The calibrated material model and the idealised loadings were then applied to a serviced-aged superheater header which was retired from service after 141,000 operational hours with around 3300 starting-up operations (flexible operation under the subcritical condition [3,4]). The main dimensions of the header are shown in Fig. 10(a), with outlet diameter and thickness of 314 mm and 33 mm, respectively [4]. The header consists of a branch-pipe and eight stub-pipes oriented at interval 36° with the vertical branch-pipe. The details of the mesh refinement for the final FE model are highlighted in Fig. 10(a), consisting

of 56,400 eight-node linear brick elements (C3D8 in ABAQUS) with a smallest element size of approximately 2 mm. A prior detailed mesh sensitivity study was conducted to establish converged viscoplastic stresses. In contrast to a significantly more refined fine mesh, only 0.1% stress difference was found relative to the chosen mesh in Fig. 10(a). Specific constraint conditions were also applied and illustrated in Fig. 10(b). The heat transfer parameters for the thermomechanical analysis, i.e. thermal conductivity and specific heat, obtained from [35] have been given in Table 4. Idealised pressure was applied to the inner surfaces, and axial pressure thrusts were applied to the stub-end and branch-end. The header under flexible operations was analysed via the anisothermal unified viscoplastic constitutive material model described in Section 3.1. A monolithic structure of the superheater header was assumed in the present work due to the lack of experimental data of the welded MarBN steel. For readers interested in the FE extension to welded branched connections via multi-material modelling, more details and references are given in the authors' previous work [6].

4.3. Smith-Watson-Topper life prediction

Multi-axial fatigue life prediction approaches can be summarized into three categories, namely equivalent stress-strain criterion, energy criterion and critical plane criterion [36]. Smith, Watson, and Topper (SWT) [37] had proposed an approach to evaluate multi-axial loading for materials with initial cracking by combining the cyclic maximum principal strain amplitude and maximum principal stress. This approach employs the maximum normal strain plane as the critical plane, which has been widely used in the service-life prediction of engineering structures. For example, O'Halloran et al. [38] recently introduced a surface damage factor in conjunction with critical-plane SWT approach to predict the minimum numbers of cycles to failure of marine risers.
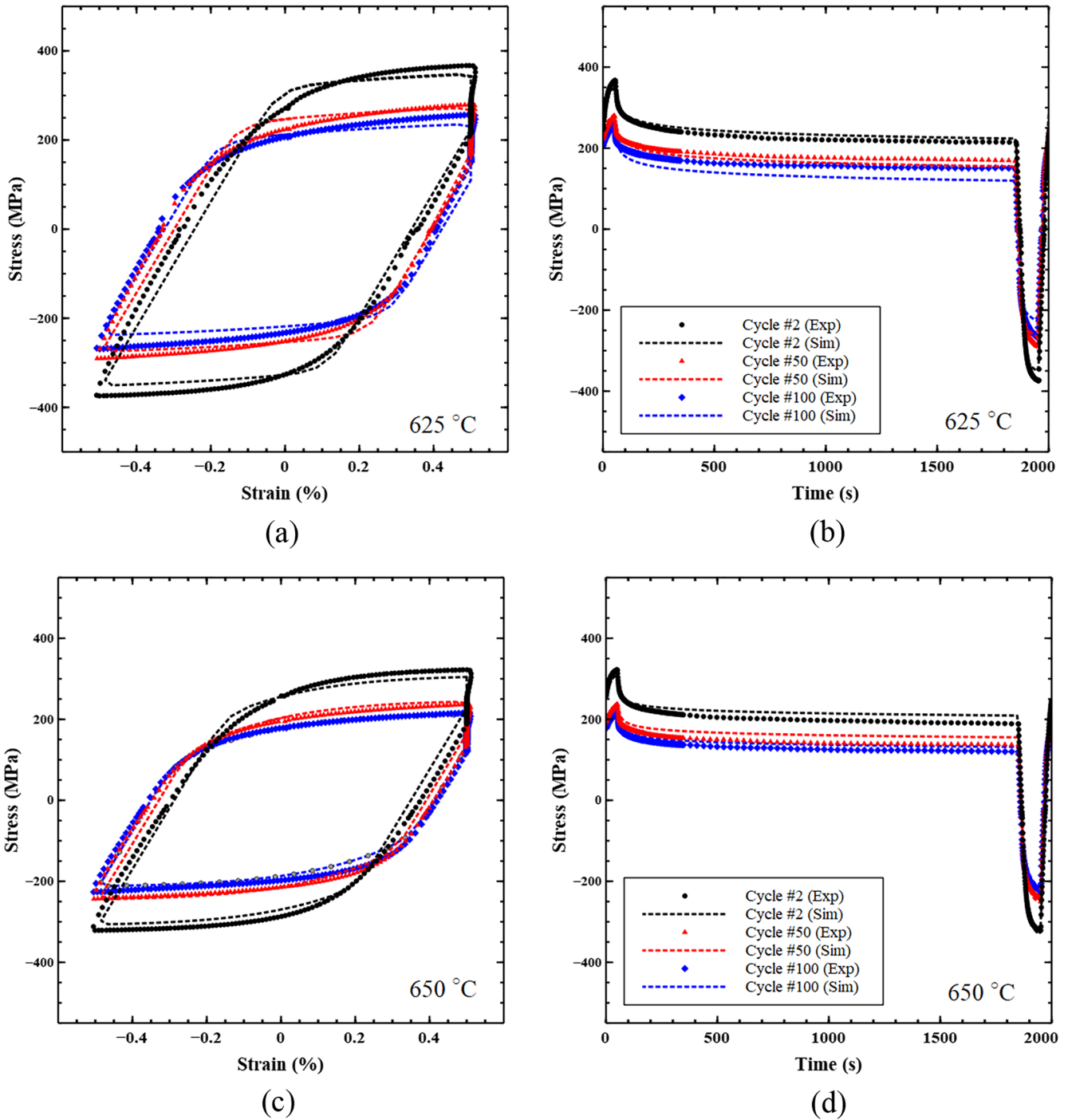
Fig. 8. The predicted and experimental hysteresis responses of the MarBN steel at 625 °C, 650 °C and 675 °C, respectively, highlighting the capability of the current model to capture the cyclic softening, the hysteresis area reduction and the stress relaxation behavior. The strain-rate was set at 0.01% s^{-1} while the hold period at 30 mins.

The form of the SWT parameter can be expressed as follows:

$$\text{SWT} = \max(0.5\sigma_{\text{I}}\Delta\,\epsilon_{\text{I}}), \tag{8}$$

where σ_{I} and $\Delta\,\epsilon_{\text{I}}$ are the maximum principal stress and maximum principal strain-range on the critical plane, respectively, which are used to estimate the component life such that

$$\max(0.5\sigma_{\text{I}}\Delta\,\epsilon_{\text{I}}) = \epsilon_f'\,\sigma_f'\,(2N_f)^{g+h} + \frac{\sigma_f'^{\,2}}{E}(2N_f)^{2g}, \tag{9}$$

where E is the Young's modulus, σ_f' and g stand for the fatigue strength and fatigue strength exponent, respectively, while ϵ_f' and h are the fatigue ductility coefficient and fatigue ductility exponent.
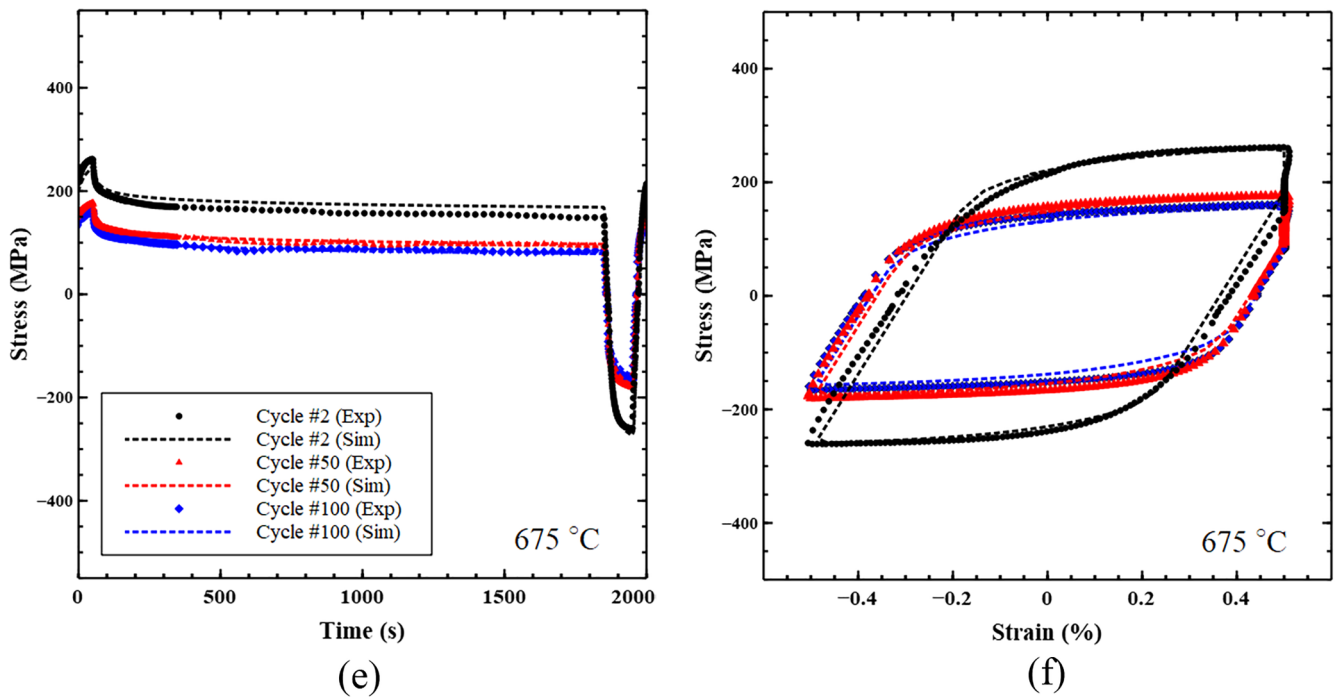
Fig. 8. (*continued*)

Table 3
The fitted equations used in the constitutive material model for the MarBN and P91 steels based on the identified material parameters at isothermal conditions.

| Parameter scopes	Material parameters	P91 [25,26]	MarBN
Elastic	Young's Modulus, E (MPa)	$-76.1\,T + 219163$	$-125.3\,T + 218950$
	Initial cyclic yield stress, k (MPa)	$-0.48\,T + 399.7$	$-1.3\,T + 968.7$
Non-linear viscosity	Viscoplastic resistance, ω (MPa.s$^{1/n}$)	$-5.76\,T + 4209$	$-3.6\,T + 2699.8$
	Viscous component, χ (–)	$0.26e^{0.0047T}$	$0.47e^{0.004T}$
Isotropic & Kinematic hardening	Saturated softening value, c(MPa)	$-0.055\,T - 29.8$	$0.6\,T - 520$
	Softening decay-rate, d (–)	$0.0035\,T - 0.55$	$0.02\,T - 12.77$
	Back-stress-1, b_1 (MPa)	$0.06\,T + 38.7$	$0.018\,T + 43.7$
	Rate of decay-1, a_1 (–)	$-0.42\,T + 3697$	$-37.7\,T + 39282$
	Back-stress-2, b_2 (MPa)	$-0.39\,T + 319.3$	$-0.14\,T + 177$
	Rate of decay-2, a_2 (–)	$-0.21\,T + 531$	$2.0\,T + 54.8$
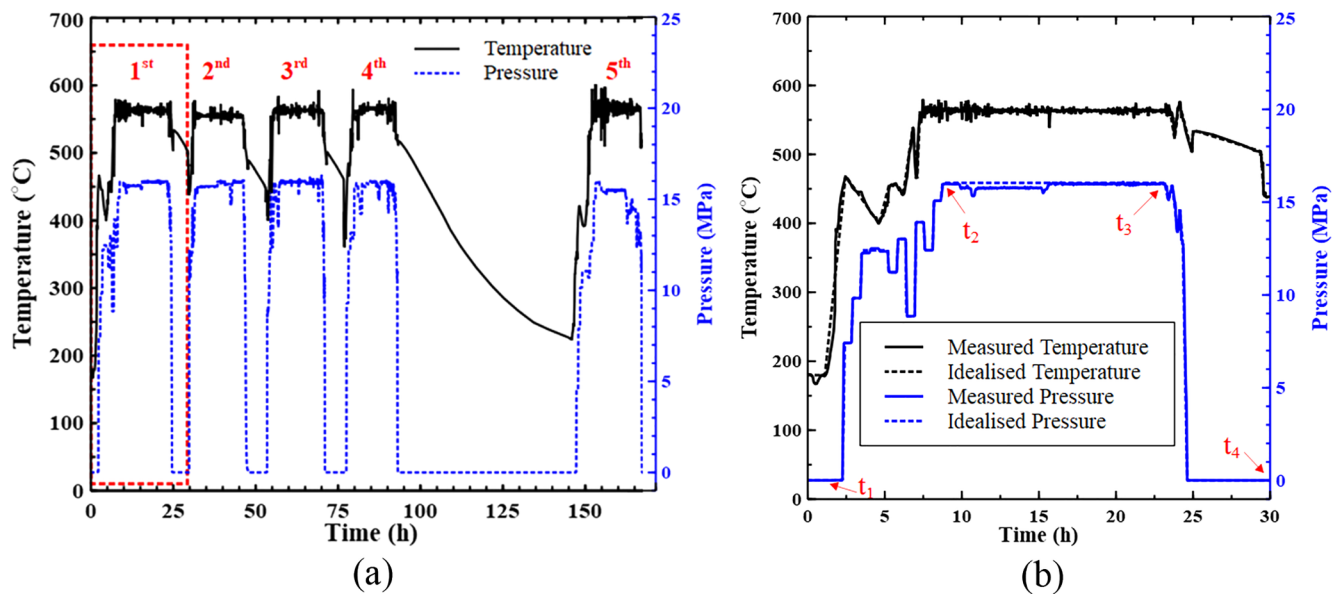
Fig. 9. (a) Operational boiler outlet steam temperature and pressure conditions for a conventional fossil-fired unit, and (b) An idealised loading profile of the 1st cycle in figure (a) used for the FE simulations.
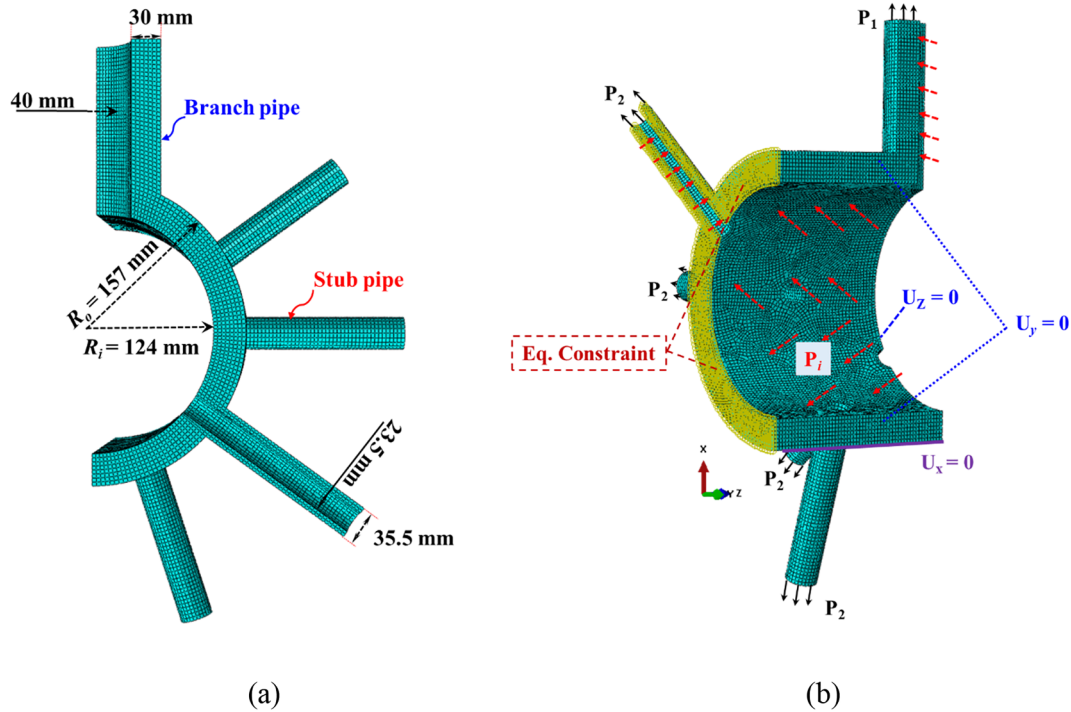
Fig. 10. (a) The FE mesh with the main dimensions of the steam header in a conventional fossil-fired power plant, (b) Boundary conditions used for the FE analyses.

Under flexible operation, the dwell period between t_2 and t_3 (Fig. 9(b)) can be regarded as the dominant phase for one representative cycle. Therefore, one can use the Coffin-Manson and Basquin constants of test data at 650 °C for the USC condition of MarBN steel and 550 °C for the subcritical condition of P91 steel in order to carry out a conservative service-life assessment of the investigated header structure under multi-axial loading conditions. The values of Coffin-Manson and Basquin parameters for MarBN steel at 650 °C and for the P91 steel at 550 °C were obtained from the experimental test data of O'Hara *et al.* [14] and R. Kannan *et al.* [39] as illustrated in Fig. 11. These parameters are given in Table 5.

5. Results and discussion

The USC condition for MarBN steel with the identified parameters is

Table 4
Temperature-dependent heat transfer parameters used in the FE model of the investigated steam header for 9Cr steels [35].

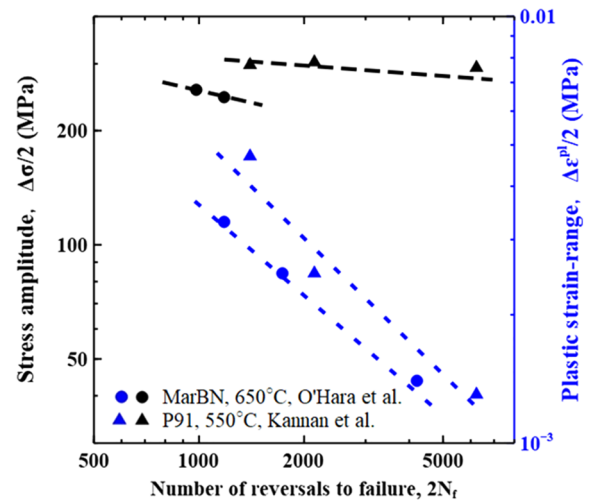| Temperature (°C)	Density g/m³	Thermal conductivity (W/m·K)	Specific heat (J/kg·K)
150	7.86	26.9	490
200		27.5	510
250			530
300			550
350		29.2	570
400			600
450			630
500		30.2	660
550			710
600			770
650			860
700		31.5	942

Fig. 11. Identification of Coffin-Manson and Basquin parameters for MarBN at 650 °C and P91 at 550 °C.

Table 5
Basquin and Coffin-Manson parameters for the MarBN steel at 650 °C and for the P91 steel at 550 °C used to assess the lifetime of the investigated header structure under multi-axial loading conditions.

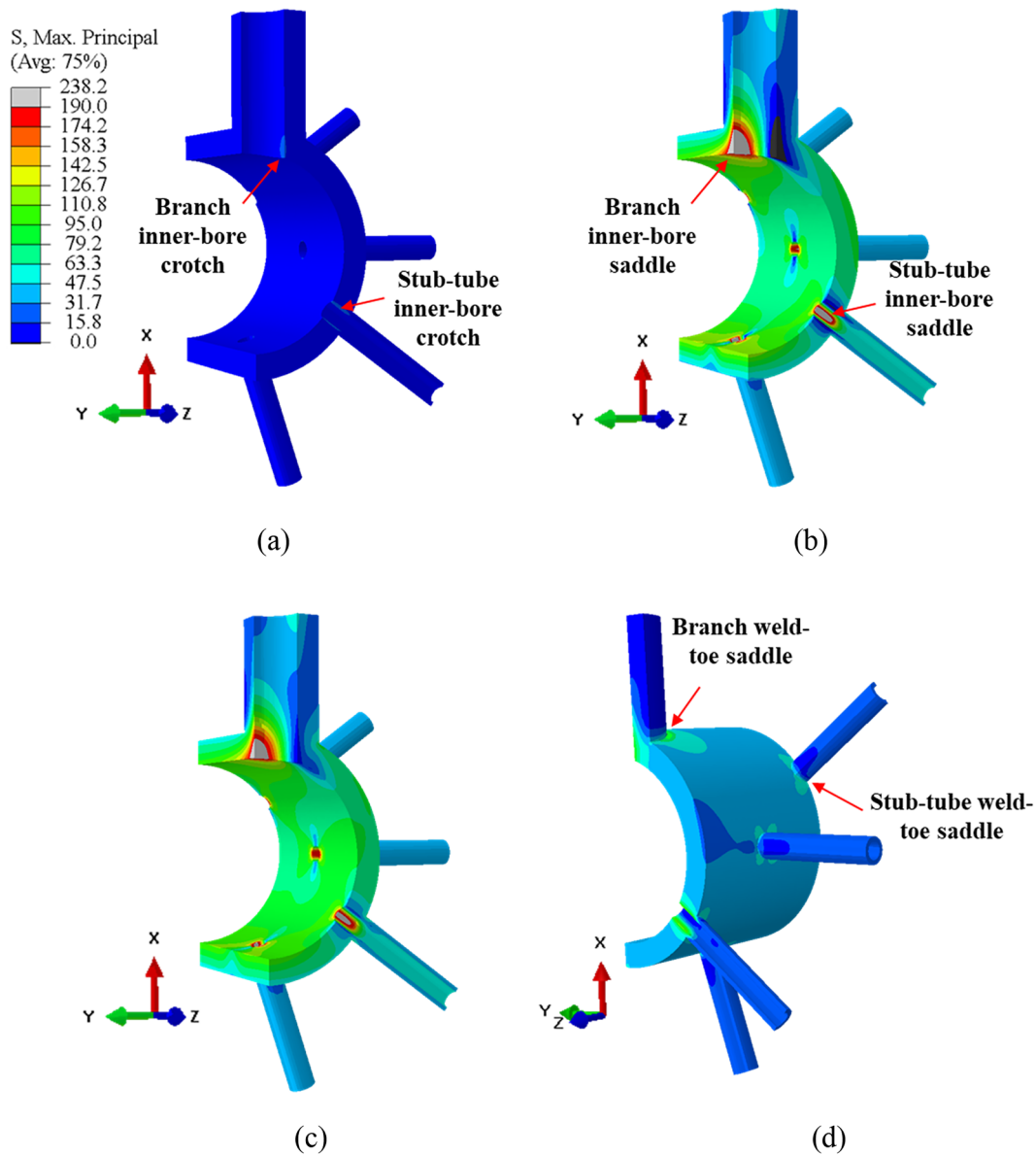| Material	Temperature (°C)	σ_f' (MPa)	g	ϵ_f'	h	E (MPa)
MarBN	650	554	−0.192	0.376	−0.386	151,151
P91	550	424.6	−0.171	0.21	−0.371	179,354

Fig. 12. Predicted spatio-temporal distributions of the maximum principal stress during the representative cycle at different selected stages as illustrated in Fig. 9(b): (a) t_1, (b) t_2, (c) t_3 and (d) t_4, for a MarBN steel header operating at USC conditions.

first adopted in order to study the viscoplastic deformation behavior and to identify the failure locations of the superheater header. To better examine the critical regions within the superheater header, the predicted contour plots for both the maximum principal stresses and viscoplastic multiplier, η, are presented in Figs. 12 and 13.

Fig. 12 shows the spatial distribution of the maximum principal stress from the USC analysis conducted on MarBN steel, which are selected at the critical time points t_1 and t_4 illustrated in Fig. 9(b). It can be seen from Fig. 12(a) that minor thermal-stress concentrations are observed at the inner-bore crotch regions of both branch-pipe and stub-pipes at the initial starting up cycle (close to t_1). With the continued pressure and temperature increasing until t_2, the peak stresses move to

the inner-bore saddle regions on the inside surface, as can be seen in Fig. 12(b). Followed by 15 h' dwell-period at full loads, the peak stress slightly decreases from ~251.9 MPa at t_2 to ~221.5 MPa at t_3 of Fig. 12(c), due to the applied stress relaxation in the constitutive material model. However, as the operation goes through the shutdown phase, a significant thermal-stress is obtained both at the inner-bore crotch regions on the inside surface and the weld-toe saddle regions on the outside surface, as illustrated in Fig. 12(d). This observation is consistent with the work reported by [5,20], where regions around the pipe penetration on the outside surface of the thick-walled header experience large thermal-stress, due to rapid changes in the steam temperature, leading to ligament cracking at sites between bore holes. It is
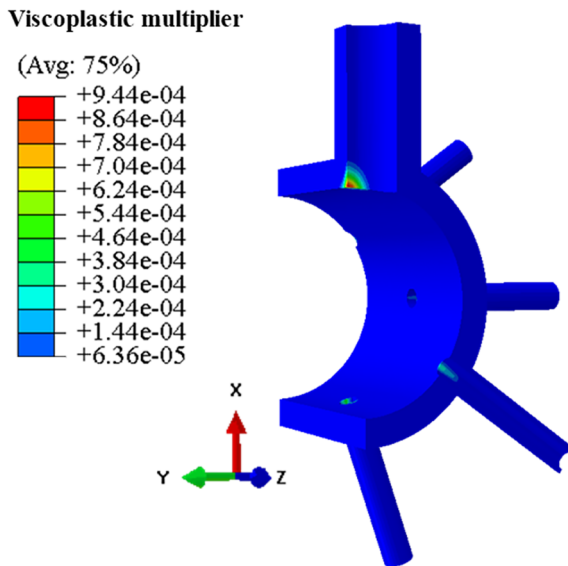
Fig. 13. Predicted viscoplastic multiplier, η, distribution at the end of representative cycle, indicating the premature failure initiates at the weld regions from pipe penetration on the inside surface.

also of great importance to investigate the viscoplastic multiplier, η, spatial-temporal distributions, as a fatigue indicator parameter for crack initiation prediction for the header component [6,20,40]. Fig. 13 shows the viscoplastic multiplier, η, distribution at time t_4 at the end of shutdown phase. It can be clearly observed that viscoplastic multiplier displays concentrated regions with dissimilar magnitudes at the inner-bore saddle regions, indicating the ligament cracking can occur in the weld regions of the pipe penetration through the shell on the inside of the header. Based on the FE analysis, inner-bore and weld-toe saddles at both branch-pipe and stub-pipe are selected for the latter service-life prediction. Noted that the superheater header of P91 under subcritical condition shows the similar distribution as shown in Figs. 12 and 13.

To further examine this issue and to quantify the trends of maximum principal stress and strain illustrated in the contour plots for the component life prediction, Fig. 14(a)–(d) present the temporal profile of the maximum principal stresses and strains during the representative cycle at the predicted critical locations, as illustrated in Figs. 12 and 13. For the branch inner-bore saddle region, the maximum principal stress shows a rapid increase to 135 MPa when the inter-pressure is around 9.6 MPa at the beginning of the heating up phase, with an initial maximum principal thermal-strain of about 0.25%. The stress then exhibited fluctuations before the loading goes through the stabilized dwell period between t_2 and t_3, as shown in Fig. 9(b) and (c). During the 15 h' hold period with maximum internal loads the maximum principal stress at the branch inner-bore saddle region decreases from ~225 MPa to ~200 MPa due to the stress relaxation induced by the introduction of viscous effect in the material model as shown in Fig. 14(a), concomitantly this effect is significantly extenuated at the stub-pipe inner-bore saddle region, see Fig. 14(c). However, the similar stress relaxation behavior cannot be observed at the weld-toe saddle regions of branch-pipe and stub-tubes during the short hold period as illustrated in Fig. 14(b) and (d). Significant thermal-strain can be observed at all

regions during the shutdown phase, almost twofold larger than the magnitudes of the initial heating up phase. Similar tendencies are observed for the P91 header at these locations under the same loading patterns of the subcritical condition, as illustrated in Fig. 15. The predicted maximum principal stress and strain-range at the four locations in Figs. 14 and 15 is coupled with SWT approach to assess the fatigue crack initiation (FCI) of headers, which gives a reasonable comparison with industrial experience as tabulated in Table 6 on the assumption of 292 starting-up cycles per year.

6. Conclusions and future work

A temperature-dependent unified viscoplasticity model incorporating the interactions of the viscous effect with cyclic softening and kinematic hardening is presented in this work and applied to the multi-axial modelling of a critical fossil-fired power plant component. The proposed methodology successfully links the idealised loading histories of flexible operation at high temperature, uniaxial high temperature experimental fatigue data, and SWT approach together, in order to predict the potential premature failure locations and estimate the lifetime at component level compared with the industrial report. The key conclusions obtained are:

- Identification and calibration of cyclic constitutive viscoplastic parameters of MarBN from uniaxial high temperature LCF and CFI experimental tests over a range of temperatures coupling with the unified viscoplasticity model have facilitated new insights into the mechanical deformation behaviors of MarBN component in the power plant under flexible thermomechanical operations for future application.

- The predicted results under both subcritical and USC conditions indicate that initial thermal-stress and strain of header concentrate at the inner-bore crotch regions during the heating up phase, while these regions migrate to the inner-bore saddle regions on the inside surface when the operation comes into stabilized phase. The stress relaxation effect can only be observed at inner-bore saddle regions. During the shutdown phase, the thermal-stress and strain concentration are found to be located at the inner-bore crotch regions and the weld-toe saddle regions. The branch inner-bore saddle region is shown to be more detrimental in contrast with the regions at stub-pipes.

- The FCI of P91 header under subcritical condition is shown to correlate well with the industrial experience at the most critical location of branch inner-bore saddle. In addition, The FCI on the outside surface is predicted to be longer than that of the inside surface. The header of MarBN under USC condition is shown to have a comparable service-life performance compared to P91 header under subcritical condition even the maximum operating steam loading increase significantly.

- The occurrence of the weldments is detrimental to the service-life of the power plant connections due to the thermal-gradient induced material inhomogeneity [41]. Thus, it is important in our future to experimentally characterize the microstructure features, as well as the mechanical properties for the welded MarBN through small-scale test [41–43], coupled with our physical modelling technics [41] to enhance the fundamental understanding of the high temperature performance of 9Cr steels.
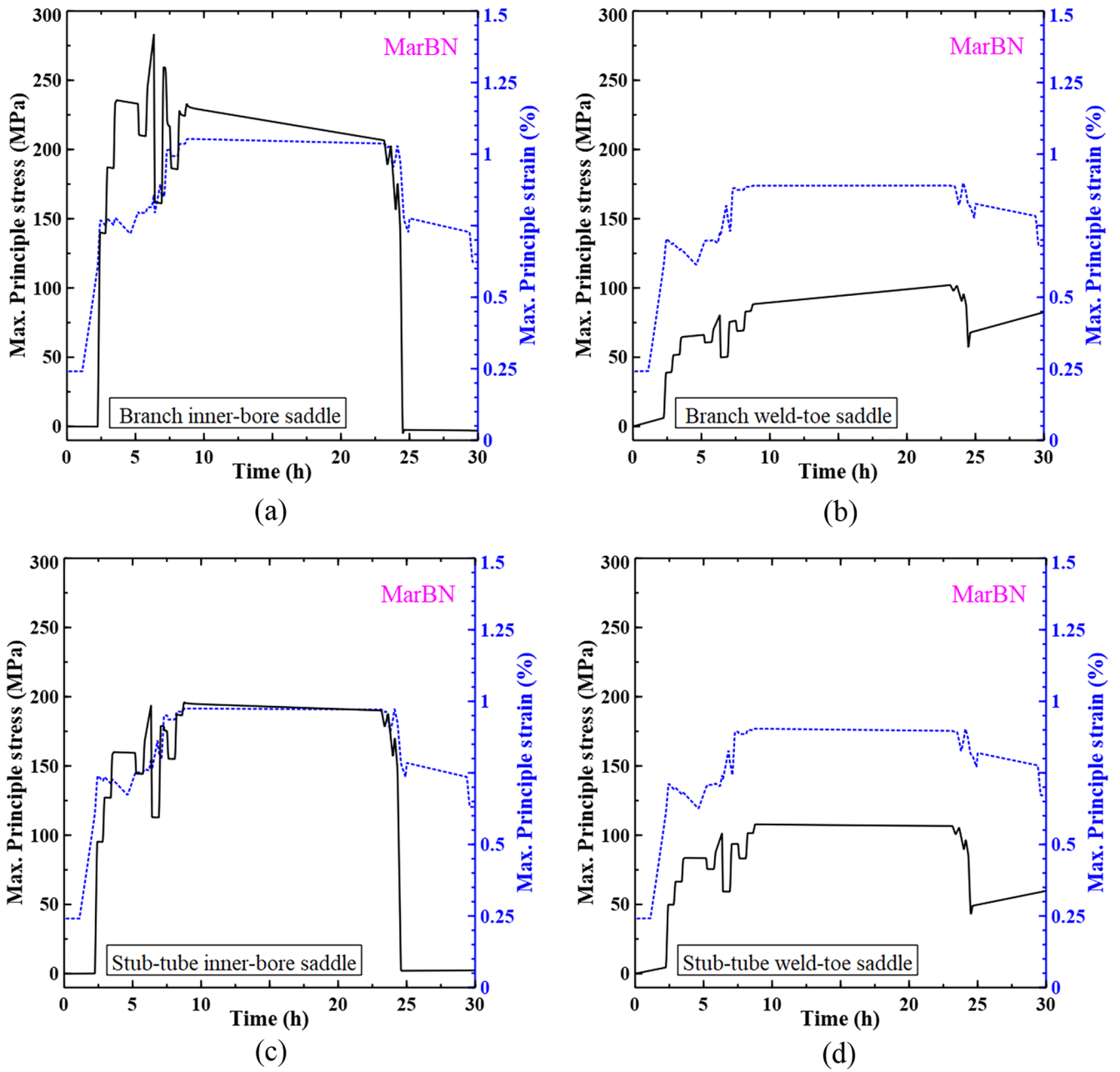
Fig. 14. Maximum principle stress and strain temporal evolutions for the MarBN under the USC condition with the same loading pattern as shown in Fig. 9(b): (a) and (b) for branch inner-bore and weld-toe saddle regions, (c) and (d) for stub-pipe inner-bore and weld-toe saddle regions, respectively.

Fig. 15. Maximum principle stress and strain temporal evolution for the P91 header subjected to the subcritical condition for loading pattern as given in Fig. 9(b): (a) and (b) for branch inner-bore and weld-toe saddle regions, (c) and (d) for stub-pipe inner-bore and weld-toe saddle regions, respectively.
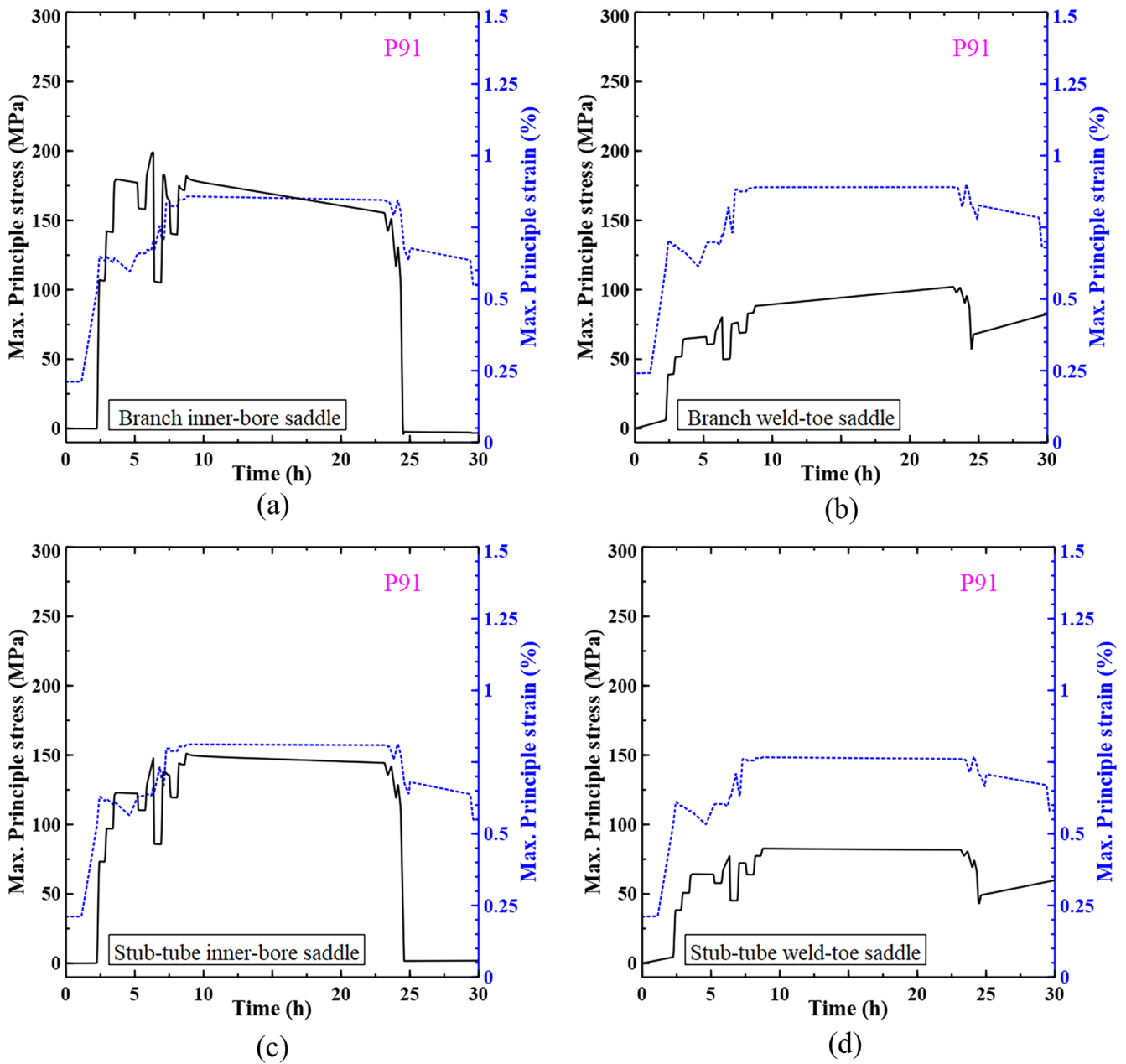
Table 6
Life prediction of headers for FCI at different locations for both 9Cr steels under the subcritical and USC conditions using the SWT approach.

Material	Conditions	Header	Locations	FCI (cycles)	FCI (years)	Unit Avg. life (years)
MarBN	USC	Branch-pipe	Weld-toe saddle	21,995	75.3	–
			Inner-bore saddle	2734	9.36	
		Stub-pipe	Weld-toe saddle	19,754	67.6	
			Inner-bore saddle	6009	20.9	
P91	subcritical	Branch-pipe	Weld-toe saddle	19,447	66.6	16.1[4]
			Inner-bore saddle	3032	10.4	
		Stub-pipe	Weld-toe saddle	19,809	67.8	
			Inner-bore saddle	5637	19.3	

Declaration of Competing Interest

The authors declare that they have no known competing financial interests or personal relationships that could have appeared to influence the work reported in this paper.

Acknowledgments

Appendix A. Supplementary material

Supplementary data to this article can be found online at https://doi.org/10.1016/j.ijfatigue.2020.105565.

References

[1] Alizadeh MI, Moghaddam MP, Amjady N, Siano P, Sheikh-El-Eslami MK. Flexibility in future power systems with high renewable penetration: a review. Renew Sustain Energy Rev 2016;57:1186–93.

[2] Zhao YL, Fan PP, Liu M, Chong DT, Yan JJ. Fatigue lifetime estimation of a heater in coal-fired power plants under a flexible operational framework-regulating extraction steam of high-pressure heaters. Innovat Solut Energy Trans 2019;158:5225–30.

[3] Viswanathan R, Henry JF, Tanzosh J, Stanko G, Shingledecker J, Vitalis B, et al. U.S. program on materials technology for ultra-supercritical coal power plants. J Mater Eng Perform 2005;14(3):281–92.

[4] EDF company, Western Burton power plant report; 2016.

[5] Farragher TP, Scully S, O'Dowd NP, Leen SB. Development of life assessment procedures for power plant headers operated under flexible loading scenarios. Int J Fatigue 2013;49:50–61.

[6] Li M, Barrett RA, Scully S, Harrison NM, Leen SB, O'Donoghue PE. Cyclic plasticity of welded P91 material for simple and complex power plant connections. Int J Fatigue 2016;87:391–404.

[7] Li DF, Barrett RA, O'Donoghue PE, Hyde CJ, O'Dowd NP, Leen SB. Micromechanical finite element modelling of thermo-mechanical fatigue for P91 steels. Int J Fatigue 2016;87:192–202.

[8] Nagesha A, Kannan R, Sastry GVS, Sandhya R, Singh V, Bhanu Sankara Rao K, Mathew MD. Isothermal and thermomechanical fatigue studies on a modified 9Cr–1Mo ferritic martensitic steel. Mater Sci Eng: A 2012;554:95–104.

[9] Barrett RA, Hyde CJ, O'Donoghue PE, Leen SB. Thermomechanical fatigue in 9–12Cr steels: life prediction models and the effect of tensile dwell periods. Int J Fatigue 2019;126:335–45.

[10] Abe F, Tabuchi M, Semba H, Yoshizawa M, Komai N, Fujita A. Feasibility of MARBN steel for application to thick section boiler components in USC power plant at 650 °C. Proceedings of the 5th international conference on advances in materials technology for fossil power plants. 2008. p. 92–106.

[11] Barrett RA, O'Hara EM, O'Donoghue PE, Leen SB. High-temperature low-cycle fatigue behavior of MarBN at 600 °C. J Pressure Vessel Technol 2016:138.

[12] Benaarbia A, Xu X, Sun W, Becker AA, Jepson MAE. Investigation of short-term creep deformation mechanisms in MarBN steel at elevated temperatures. Mater Sci Eng, A 2018;734:491–505.

[13] Benaarbia A, Xu X, Sun W, Becker AA, Osgerby S. Characterization of cyclic behavior, deformation mechanisms, and microstructural evolution of MarBN steels under high temperature conditions. Int J Fatigue 2018;131:105374.

[14] O'Hara EM. An experimental and computational investigation of the high temperature behaviour of MarBN steel with application to effects of manufacturing. Galway: National University of Ireland; 2018. Ph.D. Thesis.

[15] O'Hara EM, Harrison NM, Polomski BK, Barrett RA, Leen SB. Fatigue damage characterisation of MarBN steel for high temperature flexible operating conditions. Part L-J Mater-Des Appl 2017;231:23–37.

[16] O'Hara EM, Harrison NM, Polomski BK, Barrett RA, Leen SB. The effect of inclusions on the high-temperature low-cycle fatigue performance of cast MarBN: experimental characterisation and computational modelling. Fatigue Fract Eng Mater

[17] Wang XW, Zhang W, Gong JM, Wahab MA. Low cycle fatigue and creep fatigue interaction behavior of 9Cr-0.5Mo-1.8W-V-Nb heat-resistant steel at high temperature. J Nucl Mater 2018;505:73–84.

[18] Zhang SL, Xuan FZ. Interaction of cyclic softening and stress relaxation of 9–12% Cr steel under strain-controlled fatigue-creep condition: Experimental and modeling. Int J Plast 2017;98:45–64.

[19] Fournier B, Salvi M, Dalle F, De Carlan Y, Caës C, Sauzay M, et al. Lifetime prediction of 9–12%Cr martensitic steels subjected to creep–fatigue at high temperature. Int J Fatigue 2010;32:971–8.

[20] Rouse JP, Zacharzewski P, Hyde CJ, Jefferson-Loveday R, Morris A, Kyaw ST. A case study investigation into the effects of spatially dependent convection coefficients on the fatigue response of a power plant header component. Int J Fatigue 2018;113:137–48.

[21] Vetri Selvan R, Sathiya P, Devakumaran K, Ravichandran G. The effect of ligament size on the thermal fatigue life of 9Cr 1Mo steel boiler header under cold, warm and hot starts. Eng Fail Anal 2019;97:727–39.

[22] Islam N, Dewees DJ, Cooch M, Hassan T. Creep-fatigue damage evaluation of modified grade 91 headers using damage coupled unified viscoplastic model. ASME pressure vessels and piping conference. 2017.

[23] Li DF, Golden BJ, O'Dowd NP. Multiscale modelling of mechanical response in a martensitic steel: a micromechanical and length-scale-dependent framework for precipitate hardening. Acta Mater 2014;80:445–56.

[24] Sun FW, Meade ED, O'Dowd NP. Microscale modelling of the deformation of a martensitic steel using the Voronoi tessellation method. J Mech Phys Solids 2018;113:35–55.

[25] Saad AA. Cyclic plasticity and creep of power plant materials PhD. Thesis University of Nottingham; 2012.

[26] Saad AA, Hyde TH, Sun W, Hyde CJ, Tanner DWJ. Characterization of viscoplasticity behaviour of P91 and P92 power plant steels. Int J Press Vessels Pip 2013;111:246–52.

[27] Chaboche JL. Viscoplastic constitutive equations for the description of cyclic and anisotropic behaviour of metals, Bulletin de L'Academie Polonaise des Sciences. Serie des Sci Tech 1977;25:33.

[28] Chaboche JL. A review of some plasticity and viscoplasticity constitutive theories. Int J Plast 2008;24:1642–93.

[29] Benaarbia A, Rouse JP, Sun W. A thermodynamically-based viscoelastic-viscoplastic model for the high temperature cyclic behaviour of 9–12% Cr steels. Int J Plast 2018;107:100–21.

[30] Benaarbia A, Rae Y, Sun W. Unified viscoplasticity modelling and its application to fatigue-creep behaviour of gas turbine rotor. Int J Mech Sci 2018;136:36–49.

[31] Rae Y, Benaarbia A, Hughes J, Sun W. Experimental characterisation and computational modelling of cyclic viscoplastic behaviour of turbine steel. Int J Fatigue 2019;124:581–94.

[32] Abaqus. Dassault Systemes Simulia Corp; 2016.

[33] Lemaitre J, Chaboche J. Mechanics of solid materials. UK: Cambridge University Press; 1990.

[34] Abe F. Effect of boron on microstructure and creep strength of advanced ferritic power plant steels. Procedia Eng 2011;10:94–9.

[35] Yaghi AH, Hyde TH, Becker AA, Williams JA, Sun W. Residual stress simulation in welded sections of P91 pipes. J Mater Process Technol 2005;167:480–7.

[36] Das J, Sivakumar SM. An evaluation of multiaxial fatigue life assessment methods for engineering components. Int J Press Vessels Pip 1999;76:741–6.

[37] Smith KN, Watson P, Topper TH. A stress–strain function for the fatigue of metals. Defense Technical Information Center; 1970.

[38] O'Halloran SM, Connaire AD, Harte AM, Leen SB. A global-local fretting analysis methodology and design study for the pressure armour layer of dynamic flexible marine risers. Tribol Int 2020;142:105967.

[39] Kannan R, Sankar V, Sandhya R, Mathew MD. Comparative evaluation of the low cycle fatigue behaviours of P91 and P92 steels. In: 6th international conference on creep, fatigue and creep-fatigue interaction, vol. 55; 2013. p. 149–53.

[40] Sweeney CA, O'Brien B, Dunne FPE, Leen SB. Strain-gradient modelling of grain size effects on fatigue of CoCr alloy. Acta Mater 2014;78:341–53.

[41] Li M, Sun FW, Li DF, O'Donoghue PE, O'Dowd NP, Leen SB. The effect of ferrite phases on the micromechanical response and crack initiation in the inter-critical heat-affected zone of a welded 9Cr martensitic steel. Fatigue Fract Eng Mater Struct 2018;41:1245–59.

[42] Hyde TH, Sun W. Determining high temperature properties of weld materials. J. Strain Anal 2000;43:408–14.

[43] Hyde TH, Ali BSM, Sun W. Interpretation of small ring creep test data. J. Strain Anal 2013;48:269–78.